Photoacoustic 3-D imaging of polycrystalline microstructure improved with transverse acoustic waves

Théo Thréard, Elton de Lima Savi, Sergey Avanesyan, Nikolay Chigarev, Zilong Hua, Vincent Tournat, Vitali Goussev, David Hurley, Samuel Raetz

▶ **To cite this version:**

Théo Thréard, Elton de Lima Savi, Sergey Avanesyan, Nikolay Chigarev, Zilong Hua, et al.. Photoacoustic 3-D imaging of polycrystalline microstructure improved with transverse acoustic waves. Photoacoustics, 2021, 23, pp.100286. 10.1016/j.pacs.2021.100286 . hal-03411676

HAL Id: hal-03411676
https://hal.science/hal-03411676v1

Submitted on 22 Aug 2023

HAL is a multi-disciplinary open access archive for the deposit and dissemination of scientific research documents, whether they are published or not. The documents may come from teaching and research institutions in France or abroad, or from public or private research centers.

L'archive ouverte pluridisciplinaire **HAL**, est destinée au dépôt et à la diffusion de documents scientifiques de niveau recherche, publiés ou non, émanant des établissements d'enseignement et de recherche français ou étrangers, des laboratoires publics ou privés.

Distributed under a Creative Commons Attribution - NonCommercial 4.0 International License

Version of Record: https://www.sciencedirect.com/science/article/pii/S2213597921000471
Manuscript_76d423d3d2f72d4b8d490a48cf6863c4

Photoacoustic 3-D imaging of polycrystalline microstructure improved with transverse acoustic waves.

Théo Thréard[a,*], Elton de Lima Savi[a], Sergey Avanesyan[b], Nikolay Chigarev[a], Zilong Hua[c], Vincent Tournat[a], Vitalyi E. Gusev[a,*], David H. Hurley[c], Samuel Raetz[a,*]

[a] *Laboratoire d'Acoustique de l'Université du Mans (LAUM), UMR 6613, Institut d'Acoustique - Graduate School (IA-GS), CNRS, Le Mans Université, France*
[b] *Departement of Life and Physical Sciences, Fisk University, Nashville, USA*
[c] *Idaho National Laboratory, P.O. Box 1625, Idaho Falls, ID 83415, USA*

Abstract

Non-invasive fast imaging of grain microstructure of polycrystalline ceria with sub-micrometric spatial resolution is performed via time-domain Brillouin scattering. The propagation of a nanoacoustic pulse is monitored down to 8 µm deep in a 30×30 µm^2 area. Grains boundaries are reconstructed in three-dimensions via a two-step processing method, relying on the wavelet synchro-squeezed transform and the alphashape algorithm. Imaging contrast is improved by taking advantage of stronger sensitivity to anisotropy of transverse acoustic waves, compared with longitudinal waves. Utilization of transverse waves in the image processing reveals additional boundaries that are not discerned using longitudinal waves, confirmed by an electron backscattering diffraction pattern. A buried inclined interface between differently oriented grains is identified by monitoring changes in amplitude (phase) of the portion of the signal associated with transverse (longitudinal) waves. Estimates of the inclination angle of this interface prove the sensitivity of our laser ultrasonic method to image inclined boundaries.

Keywords: time-domain Brillouin scattering (TDBS), Picosecond acoustic interferometry, Shear-elastic-waves enhanced contrast, Inclined grain boundary, 3-D Imaging, Polycrystalline material, Asynchronous optical sampling, Wavelet synchro-squeezed transform

1. Introduction

The photoacoustic (PA) effect, light energy conversion into coherent acoustic waves was discovered in the 19th century [1], immediately followed by the suggestion of its application to spectroscopic analysis of materials. However, not until the 1980's were methodologies such as PA spectroscopy [2] and 2-D PA microscopy [3] developed as reliable materials characterization techniques. Commonly the PA technique is based on the conversion of absorbed laser light into acoustic waves via one or more energy conversion pathways, (*e.g.* thermoelastic or deformation potential piezoelectric transduction mechanisms) (Ref. [4] for a review). The detection of these generated acoustic waves is accomplished by a variety of approaches, with key examples including piezoelectric transduction and acoustic wave modulation of the phase, amplitude, or propagation direction of optical beams (Refs. [5, 6] for a review). In the case of surface light absorption, spatial resolution can be controlled by the focusing of the laser radiation [7] leading to what is called "super-resolution" [8] and to the micron, i.e. optical, scale imaging [9]. Potentially, the spatial resolution of the PA 2-D imaging could be reduced from "micro" to "nano" by applying near-field optics techniques [10]. The origin of the contrast in imaging via 2-D PA microscopy or nanoscopy is due to variation in the optic, elastic, thermal and thermoelastic parameters which could influence the conversion process of the pump light into coherent acoustic waves. Because these parameters are tied to crystalline imperfections, PA techniques provide a convenient and non-destructive approach to characterize material microstructure [11]. Most of the imaging techniques involving laser-generated coherent acoustic wave can be grouped according to their physical principles, into one of the three following categories: 1 - laser ultrasonic imaging (LUI), 2 - photoacoustic imaging (PAI) and 3 - time-domain Brillouin scattering (TDBS).

*Corresponding authors
Email addresses: threard.theo@gmail.com (Théo Thréard), vitali.goussev@univ-lemans.fr (Vitalyi E. Gusev), samuel.raetz@univ-lemans.fr (Samuel Raetz)

© 2021 published by Elsevier. This manuscript is made available under the CC BY NC user license
https://creativecommons.org/licenses/by-nc/4.0/

In the first category, imaging is achieved like in traditional pulse-echo ultrasound measurements, by launching coherent acoustic pulses (CAPs) from the sample surface into its volume, and detecting the acoustic waves transmitted/scattered by the sample inhomogeneities, defects and interfaces [12–15]. Since the scattered/transmitted acoustic waves are carrying information on the distribution of the acoustic inhomogeneities in the sample, the contrast in LUI is acoustical, and the spatial resolution with depth is controlled by the duration (length) of the laser-generated CAPs. LUI can provide nanometer scale resolution by application of picosecond or femtosecond laser pulses both for the generation and detection of picosecond duration CAPs [16–18].

In the second category, the local absorption of pump light photons penetrating in the material generates CAPs, profiled with the encoded information on the inhomogeneity of light absorption coefficient spatial distribution. The temporal shape of pulsed-laser-generated PA signal was evidenced in the 1970's to depend on the magnitude of the light absorption coefficient [19], leading the way to measure experimentally the light absorption coefficient spatial distribution from the shape of the detected CAPs (Sec. 2.2 in Ref. [4]) and applied later for biological tissues study [20, 21]. The photo-generated acoustic waves deliver the encoded information to the detection region near or on the sample surface. PAI performs 3-D imaging at centimeters to micrometers spatial scales [22–31]. In the acoustic-resolution imaging technique called photoacoustic tomography (PAT), neither the light nor the sound are tightly focused. Different implementations of PAT allow the spatial resolution to be scaled with the desired imaging depth in tissue while a high depth-to-resolution ratio is maintained [32]. PAT can achieve sub-millimeter resolution at depths up to several centimeters [32, 33].

The third category is fundamentally different compared to both LUI and PAI techniques. This approach, known under the names of picosecond ultrasonic interferometry [17, 34–36] and time-domain Brillouin scattering (TDBS) [36], is based on the interaction of probe light with CAPs propagating inside media that are transparent or semi-transparent at the probe wavelength. TDBS and frequency-domain Brillouin scattering differ by the physical origin of the acoustic waves scattering the probe light. Unlike frequency-domain Brillouin scattering, which involves light scattering from incoherent thermal phonons existing in each point of the media and propagating in all directions, TDBS involves light scattering from highly directional CAP beams. The parameters of the CAP beam, such as its frequency spectrum and the directivity pattern, can be controlled like in LUI, via the design of the optoacoustic transducers (OAT) and the choice of the pump light characteristics and optical focusing [4, 36–38]. Application of ultrashort laser pulses, of picoseconds duration or shorter, provides opportunity to launch coherent acoustic waves in the GHz frequency range. The coherent acoustic waves compose the CAPs, as small as nanometers to sub-micrometers length, that are obtained when the laser pulses are incident on either strongly absorbing materials (like metal or semiconductors with light penetration depths shorter than several tens of nanometers) or just nanometers thick absorbing films/coatings on the transparent substrate. This length scale controls the axial (depth) dimension of the probe light scattering volume, *i.e.* the dimension along the propagation direction of the CAP. The lateral dimensions of the scattering volume are controlled by the focusing of the pump light, because it determines lateral dimensions of the launched coherent acoustic beam and the angular spectrum of the emitted CAPs [4, 39].

3-D imaging by TDBS is achieved by scanning the co-focused pump and probe laser beams along the surface of a sample. The lateral resolution is controlled by the overlapping pump and probe foci. TDBS was first successfully applied to imaging in transparent media with spatially localized inhomogeneities [40–44]. Following these seminal studies, the TDBS technique has been extended to 2-D and 3-D imaging of the continuously distributed inhomogeneities in nanoporous materials [45, 46], ion-implanted semiconductors and dielectrics [47–49], texture in polycrystalline materials [50, 51] or inside vegetable and animal cells [52–54], and temperature profiles in liquids [55]. All these experiments confirmed that, when the CAP is reflected/transmitted by an interface between two transparent media, a TDBS signal can change both

in periodicity and amplitude. Changes in periodicity are due to different acoustical and different optical properties in each medium. Amplitude changes are additionally due to different acousto-optical parameters in each medium as well as acoustical and optical impedance mismatches across interfaces. The characterization of the spatial orientation of plane interfaces or, more generally, imaging of complex non-plane interfaces by TDBS in the bulk of a medium, has emerged quite recently in relation to polycrystalline materials with application in the energy industry [56–58], following earlier experiments where the surface acoustic waves generated and detected by ultrafast lasers were applied for the imaging of grain boundaries on the surface of a medium [59].

In Ref. [56], a 2-D image of a subsurface grain boundary in a polycrystalline UO_2 sample was obtained due to the variations of both the frequency and the amplitude of a monochromatic Brillouin oscillation, when CAP was crossing the boundary. In [57], the 3-D TDBS imaging was applied to the evaluation of the elastic constants of CeO_2 and determination of the crystallographic orientation of the grains on the surface of the sample. It was demonstrated that TDBS imaging with a quasi-transverse acoustic (TA) pulse can be more sensitive to grain orientation than TDBS imaging with quasi-longitudinal acoustic (LA) pulse. 3-D orientation of the subsurface boundary by TDBS imaging with LA mode was also reported. Finally, it has been demonstrated very recently [58] that complete orientation of the surface grains can be obtained by measuring how the polarization of the probe beam influences the detected signal amplitude in the TDBS imaging. These recent studies on imaging grain microstructure with TDBS lead to the ability of 3-D imaging of grains and grains boundary in large volumes of polycrystalline materials. Yet, the complete 3-D imaging in a large volume (about 7 200 μm^3 here) remains to be addressed, due to the current lack of a dedicated and robust signal processing analysis routine and image reconstruction procedures. In this manuscript we present a method for efficient and complete 3-D image reconstruction of grain microstructure in polycrystalline CeO_2.

The CeO_2 sample and the experimental scanning system are described in Sec. 2. TDBS is introduced and the step-by-step processing of the TDBS signals is detailed, from the photodiode measurements to the 3-D imaging results. In Sec. 3, the 3-D imaging results are presented. The contribution of the transverse acoustic waves reveals "new" grains via higher contrast. An inclined interface is uncovered, buried below the free surface of the sample, and its angle of inclination with respect to the surface is estimated. Limitations of the method to untangle the different contributions to the TDBS signal at the interface are discussed. The conclusions are stated in Sec. 4.

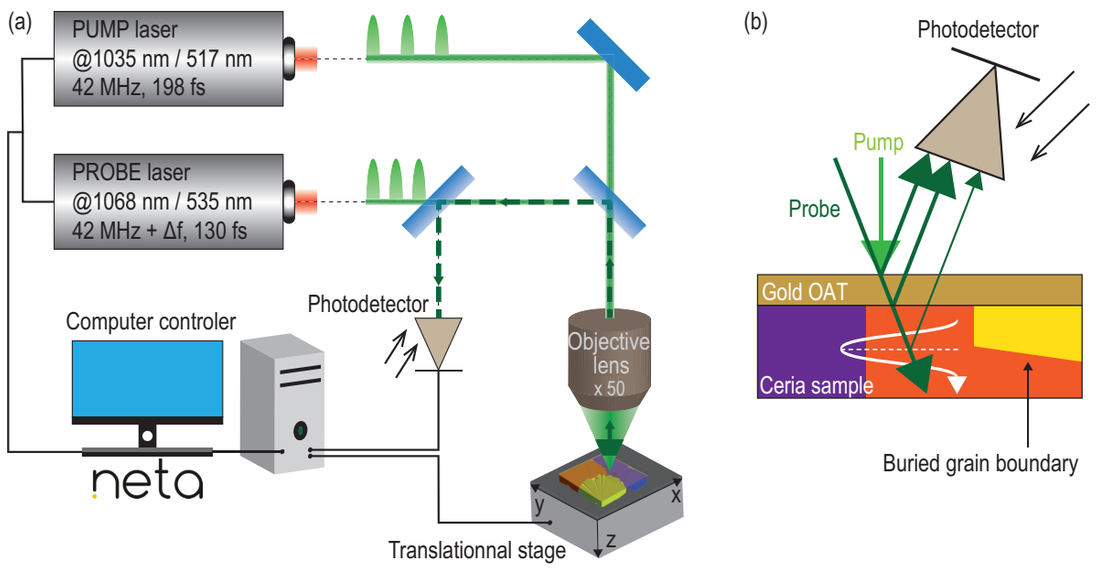

Figure 1: (a) Schematic of the experimental TDBS imaging system (JAX-M1) commercialized by NETA (France). b) Schematic of the probe beam reflections in TDBS (reflection configuration): two stationary reflections occur at the OAT interface, while a third weaker reflection occurs at different depth along the propagating path of the acoustic pulse. A buried inclined boundary between two grains is represented in the right part of the polycrystal's schematic. (colors needed)

2. Materials and Methods

2.1. Sample and experimental setup descriptions

The sample studied is a cubic polycrystalline cerium dioxide (or ceria) CeO_2, with an optical refractive index $n = 2.37$ at probe wavelength $\lambda = 535$ nm, estimated from the measurements (in good agreement with [60], see appendix for details). The sample was annealed at 1650°C to promote grain growth (see Ref. [57] and supplementary materials for details), the average grain size being ∼20 microns. A focused ion beam was used to put down fiducial marks. The crystallite orientation was obtained using electron backscatter diffraction. The fiducial marks are visible optically and in the EBSD micrograph and are used to locate specific grains. A 20 nm-thick gold layer was coated to serve as an opto-acoustic transducer (OAT). Ceria, which is optically isotropic and elastically anisotropic because its crystalline structure is cubic, provides a model material for demonstrating enhanced imaging using transverse acoustic waves, without the complication of optical birefringence. In the case of birefringent materials, *i.e.* optically anisotropic crystals, polarimetry measurements would be required to distinguish ordinary from extraordinary light contributions to the TDBS signal. Moreover, refraction of the probe light at the interface between differently oriented grains would modify the scattering efficiency in the deepest grain, while in the presented case there is no refraction of light at the interface.

Measurements of the transient reflectivity signals were done using a pump-probe Asynchronous Optical Sampling (ASOPS) system: the JAX-M1 commercialized by NETA [61–63] [Figure 1 (a)]. The setup is composed of two Yb:KYW mode-locked laser cavities, emitting femtosecond laser pulses. The pulse delay between the two lasers is accomplished electronically by changing the pulse repetition rate of replica laser keeping the source laser repetition rate fixed. The difference in the frequency of repetition between the two lasers, or the beat frequency, is set to $\Delta f = 500$ Hz. Both pump and probe beams are focused, using a $\times 50$ microscope objective lens, on the free surface of the gold coated sample. Only the second harmonics of the laser sources are used. The wavelength of the probe is $\lambda_{\text{probe}} = 535$ nm, while that of the pump is $\lambda_{\text{pump}} = 517$ nm. To monitor the relative optical reflectivity change $\Delta R/R$ caused by the propagating CAP, the backscattered probe light is directed to a photodiode where it interferes with static reflections of the probe beam on the sample surfaces [Fig.1(b)]. The automatic scan and signal acquisitions are realized using NETA's built-in software. More details on the ASOPS-based setup can be found in [61]. The sample being placed on a displacement stage, and due to the speed of a single-point measurement, a scan lasting less than five hours is realized on a 30×30 µm^2 zone, with a lateral resolution of 0.469 µm. Probed depth reaches 8 µm in the most favorable cases, with an axial (*i.e.* along the depth) resolution of about 0.75 µm (more details on depth of imaging can be found in the supplementary materials).

2.2. Time-domain Brillouin Scattering (TDBS)

The TDBS method aims to study materials, transparent or partially transparent to the wavelength of the probe laser beam λ_{probe}, by monitoring the propagation of a coherent acoustic pulse (CAP), generated in the OAT by the pump laser pulse. The thermo-elastic mechanism is responsible for acoustic wave generation: the pump laser pulse is focused on the surface of the OAT, inducing a fast temperature rise (heating) hence deformation of the material by thermo-elastic stresses. This process generates acoustic waves that can be considered plane (large lateral-distribution-to-acoustic-pulse-length ratio) and that propagates in the OAT, normally to the free surface, and reach the interface OAT/CeO_2, where the acoustic waves are transmitted in ceria. In our case, the time-delayed probe laser pulse is focused on the same side as the pump laser.

In the TDBS imaging experiments reported here, a portion of the probe light reflected from the propagating CAP is measured via heterodyning with the portion of the probe light reflected from the OAT [Figure 1 (b)]. This Brillouin scattering of probe light contributes to the total variations of the transient reflectivity and gives rise to an oscillating component in time, due to the interferences with stationary scattered light. Periodicities of these oscillations are related to the phase shifts acquired by the probe light when scattered

from the acoustic pulses travelling in the media. For a probe beam parallel to the direction of the acoustic pulse propagation, the frequency f_B of the Brillouin oscillations is linked to the velocity v of the propagating pulse optical refractive index n at probe wavelength, by:

$$f_B = \frac{2\ n\ v}{\lambda_{probe}}\ . \tag{1}$$

When depth profiling with TDBS, the information from different spatial positions along the acoustic pulse propagation path inside the sample is obtained. The phase of the probe light scattered by the CAP contains the information on the product of the local optical refractive index by the local acoustic velocity [17, 34, 36, 45, 46, 64]. The amplitude of the scattered light also contains localized information on the components of the photo-elastic tensor, which determines the strength of acousto-optic interaction [36, 46, 47, 65, 66].

Three acoustic quasi-modes can be launched in the elastically anisotropic ceria: a quasi-longitudinal acoustic (LA), a "slow" transverse acoustic mode (sTA) and a "fast" transverse acoustic mode (fTA). Generation efficiency of transverse acoustic waves has been recently studied in Ref. [67]. By considering multiple crystallite orientations, an estimate of the Brillouin frequency (BF) range can be obtained for each acoustic mode (Table 2). More details on the computation of this BF intervals are given in the supplementary materials. In the following, transverse modes with frequencies falling in the common BF interval $[26.79 - 37.97]$ GHz are labeled as TA, while modes above this interval can be unambiguously labeled as fTA modes.

Table 1: Expected Brillouin frequency (BF) intervals to be detected with TDBS in the case of cubic ceria CeO_2, for each acoustic quasi-modes, using elastic properties and density from [57, 58]

Acoustic mode	Frequency interval (GHz)
LA	[58.77 - 70.02]
sTA	[26.79 - 37.97]
fTA	[26.79 - 42.48]

2.3. On the processing of transient reflectivity signals

The raw transient reflectivity signals are processed as follows. First they are filtered in order to isolate the acoustic contribution (oscillating part of the signal) from the total transient reflectivity. A three-steps procedure starts by denoising the raw transient reflectivity signals with a 48th-order finite impulse response (FIR) bandpass filter with a passband in the range [25 - 75] GHz tuned to the expected BF of table 1. The initial "electronic" peak in the signals, corresponding to the overlapping time of both pump and probe laser pulses, is removed since it is not related to the acoustic contribution. The first 14,3 ps are cut to remove the electronic response near t = 0 ns, meaning that the first nanometers in contact with the gold nanolayer (OAT) are not used (*i.e.* considered homogeneous) for the depth vector reconstruction. Finally, to estimate and subtract the remaining contribution of the thermal processes, we apply a local linear regression method (LOESS from MATLAB) over 500 points (0.24 ns) to the filtered peak-free signal. This treatment is applied to all the 3600 signals of the scan presented in this paper. The signals coming out of these three steps of filtering, referred to as the "acoustic signal", are considered to contain exclusively the acoustic contribution of the signals and are further processed as discussed in the following.

2.4. On the processing of the acoustic signals: slicing

The slicing of each acoustic signal, to study the evolution of their frequency content as a function of time, is performed via the wavelet synchro-squeezed transform (WSST) [68, 69]. This tool aims to narrow the time-frequency representation obtained with the wavelet transform by re-allocating the spectrum energy along the frequency axis only. Such WSST tools are used, in combination with ridge extraction, to reconstruct the temporal behaviour in time of a superposition of AM/FM modes, in a noisy signal [70, 71]. Applications to paleoclimate datas [72] showed the robustness of this method, now extended to a variety of

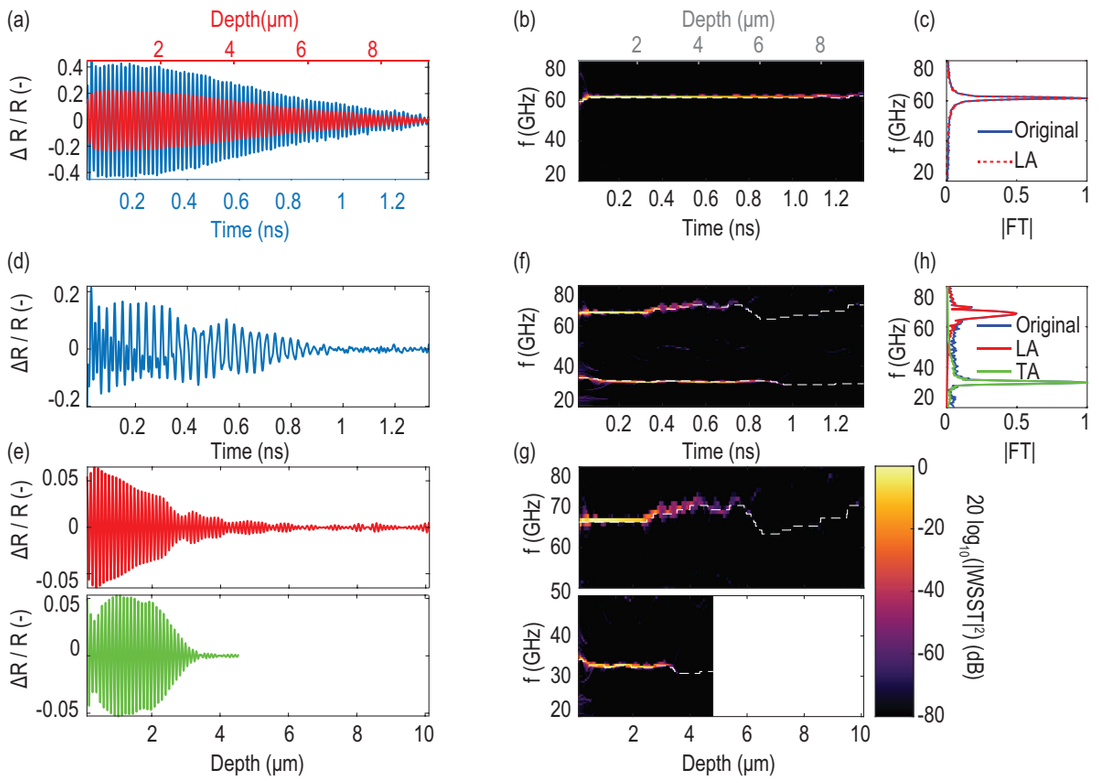

Figure 2: Analysis of two typical acoustic signals of the scan (a-c) and (d-h). (a) Acoustic signal (blue signal and x-axis) and reconstructed LA contribution (red signal and x-axis) of the signal located at coordinates (25.79 µm, 23.45 µm) in the scan. (b) Associated WSST and extracted ridge (dashed white line on the spectrogram). (c) Associated Fourier Transform (FT) of the full signals of (a). (d) Acoustic signal located at coordinates (9.38 µm, 11.72 µm). (e) Reconstructed LA (red, upper) and TA (green, lower) contributions to the acoustic signal (d). (f) Associated WSST and ridges (white dashed lines on the spectrogram) of the acoustic signal (d). (g) Associated WSST and ridges (white dashed lines on the spectrogram) of the reconstructed LA (red) and TA (green) contributions (e), zoomed on the frequency of interest. (h) Associated Fourier Transform (FT) of the full signals (d) and (e) related by their colors. The depth vectors are reconstructed from the instantaneous frequency of the ridge extracted from the associated acoustic mode and Eq. 1, explaining the "downsizing" of the slower TA mode in the lower part of (e) and (g). (colors needed)

signal decomposition problems [73, 74]. Performing a ridge extraction, extraction of the maximum-energy time-frequency ridge of the spectrum, offers the possibility to evaluate with precision the BF of the acoustic mode studied, for each time step. The elegance of the WSST is found in its capacity to offer a clear enough spectrum so that 3 ridges extraction can be performed, as long as these ridges are sufficiently separated in frequency (refer to the definition 3.2 on intrinsic mode components separation in Ref. [68] for further details). The ridge is extracted along the full measurement time, but only the points of the ridge with energy amplitude over a -68 dB threshold value are kept.

For example, the reconstruction of a single-frequency signal is depicted in Fig. 2(a). The acoustic signal measured at the position (x, y) =(25.79 µm, 23.45 µm) in the scan is represented in blue (with associated x-axis in blue); and the signal in red (with associated x-axis in red) correspond to the contribution of the LA mode to the acoustic signal. The temporal behavior of LA mode contribution is reconstructed from the ridge extracted in the spectrogram obtained with the WSST [Fig. 2(b)] by applying the inverse WSST (IWSST). The LA mode contribution is plotted with respect to depth, the depth vector being reconstructed with Eq. 1 and the instantaneous frequency, *i.e.* local velocity, of the extracted ridge. The Fourier Transform (FT) of both full signals [Fig. 2(a)] confirms the presence of a single-frequency component, corresponding to the monitoring of a long-lasting LA mode. Another signal, located at the position (x, y) =(9.38 µm, 11.72 µm), is given in Fig. 2(d). This signal contains two distinctive frequencies, confirmed by its WSST spectrum [Fig. 2(f)], sign that two different acoustic waves are monitored. The contributions to the acoustic signal associated to the two modes are plotted with respect to the reconstructed depth in 2(e), the contribution of the LA mode being in the upper part in red, and the one of the TA mode in the lower part in green. The

depth vector of both modes are reconstructed thanks to Eq. 1 and their associated instantaneous frequency in the extracted ridges of their WSST spectra [Fig. 2(g)]. Velocities of the TA waves are predicted to be nearly two times slower than the velocity of the LA waves, explaining the two-times shorter depth of reconstruction of the TA mode (lower part of Fig. 2(e) and (g)). Finally, the FT [Fig. 2(h)] of all the signals [Fig. 2(d-e)] confirms the presence of the two modes and their good frequency separation during the reconstruction.

Knowledge of the BF of the acoustic mode for each time step allows the conversion from time to depth using Eq. (1). For each time step, the acoustic wave velocity associated with the extracted BF allows an estimate of the travelled depth since the previous time-step. The time-frequency ridge extracted from one acoustic mode of one signal becomes a depth(z-axis)-frequency ridge. Assembling all the depth frequency ridges of the 3600 signals of the scan, for one of the three possible acoustic quasi-mode, leads to a 4-D "sliced" representation of the complete set of collected data.

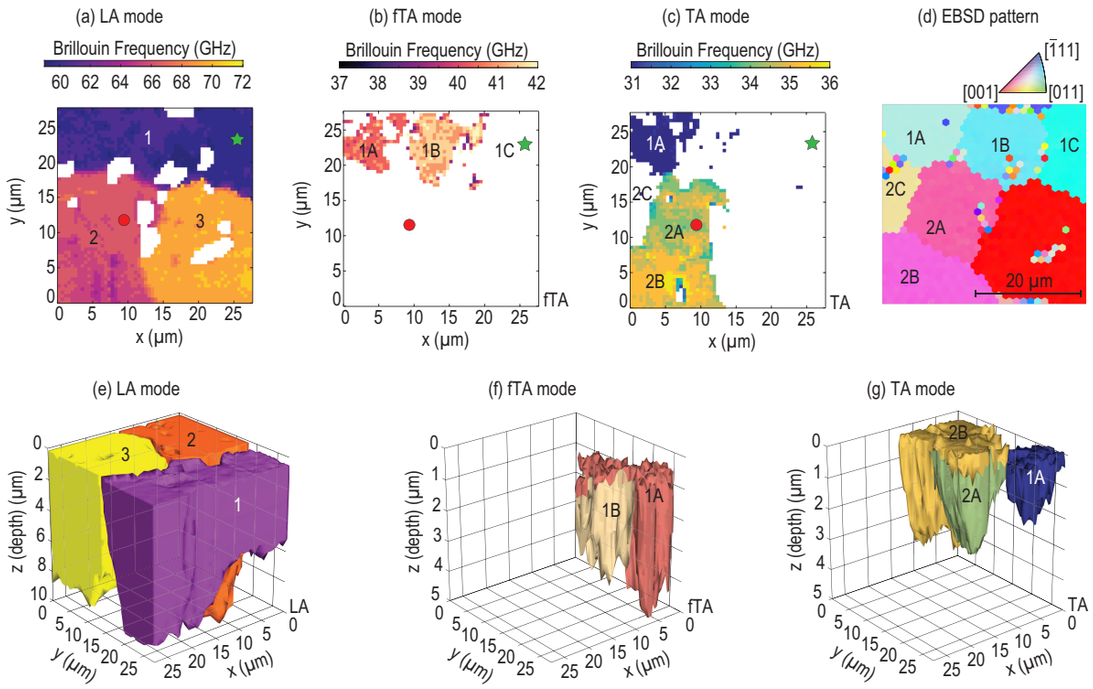

Figure 3: Imaging results: upper view (free surface of the sample) of the slicing output for each BF interval [Tab. 1] (a-c), electron backscattering diffraction (EBSD) pattern of the scanned area (d), and 3-D alphashape representations (e-g) of the associated (color and order) BF interval (a-c). Showing the upper view of the 4D "stacked" representation from the slicing processing step of the (a) LA, (b) fTA and (c) TA modes (colors associated to the BF) offers the possibility to appreciate the good agreement between the first slices and the EBSD pattern (d). The positions of the previously analysed signals are represented by a green star [Fig. 2(a-c)] and red circle [Fig. 2(d-h)]. The alphashape results evidence the reconstitution of 3 grains (1/purple, 2/orange and 3/yellow) with the LA mode (e), 2 grains (1A/salmon-red and 1B/beige) with the fTA mode (f) and 3 grains (1A/blue, 2A/green and 2B/yellow) with the TA mode (g). One can identify how TA modes allows to identify smaller grains from bigger homogeneous ones imaged by LA modes. (colors needed)

2.5. On the processing of the acoustic data: shaping

From the 4-D output of the slicing step (Sec. 2.4), one voxel is defined by its BF and its 3-D location (x,y,z). A grain is thus defined by a group of adjacent voxels with common BF. To form a grain, it is assumed that the corresponding group of adjacent voxels should be composed of at least 5% of the total voxels of the 4-D stacked representation for each mode. The 5% threshold allows to denoise the final 4-D representation of grains, with the drawback of removing small grains from the image. Typically, in the case of LA mode, the total volume occupied by the voxels after thresholding the ridge extraction in the slicing step reduces from 7 200 µm^3 to about 4 800 µm^3 (Tab. 2). This means that grains with a volume less than approximately 240 µm^3 are neglected in the LA reconstruction due to the 5% threshold. Note that in the case of the fTA mode, the volume occupied by the voxels after thresholding is 450 µm^3, thus the minimal

volume of a grain in that case is of about 23 µm^3, while in the case of TA mode, the volume occupied by the voxels is 680 µm^3, hence the minimal grain volume is of about 34 µm^3. These estimates seems to be acceptable in our case since grains are expected to have larger volumes, the smallest grain being depicted by the blue grain reconstructed by TA detection in Fig. 3(g). The number of grains, and the associated BF intervals bounding the gathered voxels, are estimated via a segmentation method inspired from Otsu's work (details can be found in supplementary materials) [75]. This method identifies each cloud of voxels containing common BF that are used as an input to the alphashape algorithm [76, 77]. This algorithm relies on a constraining parameter $1/\alpha$, linked to the radius of a sphere, to shape convex and non-convex envelope of the cloud of voxels. Hence an infinite radius leads to the convex hull of the cloud of voxels, while a zero radius gives the cloud of voxels itself (no envelope). The different envelopes obtained between these two particular cases are named the family of alphashapes of the cloud of voxels. In the following analysis, the radius is set as twice the lateral spatial resolution of the scan, thus $1/\alpha = 1$ µm. The shaping of each cloud of voxels containing common BF-segmented interval offers a volumetric representation of all the boundaries of a single grain (see Fig. 3 and related discussions in the following section).

3. Results and discussion

3.1. 3D imaging enhanced with transverse waves

The signal shown in Fig. 2(a), which corresponds to a grain with no subsurface boundaries within the interrogation volume, is used to assess the maximal depth of imaging of our system. This depth is ∼8 µm, attributed to the TDBS imaging coherence penetration depth of the probe laser (details in supplementary materials). The signal shown in Fig. 2(d) offers insight into multi-component signals with BF in the LA mode interval as well as in the TA mode interval. The reconstruction of the temporal behavior [Fig. 2(e)], and its change with depth, associated with both acoustic modes gives the opportunity to extract complementary information used for the imaging. The boundary between two differently-oriented grains is evidenced by the two modes via two different physical mechanisms. First, the LA mode is subject to an upshifting of its BF [Fig. 2(g)] that can be attributed, following Eq. 1, to the increase of the LA mode velocity due to its transmission to a differently-oriented grain. In parallel, the TA mode amplitude suddenly decreases to the noise level [Fig. 2(e,g)] at the same corresponding depth (∼3 µm) at which the BF of the LA mode is upshifted. This sudden drop in amplitude of the TA mode after transmission into the second, subsurface grain is the signature of: either large angle, off-axis refraction of the TA mode such that the interaction with the probe is vanishingly small, or small photoelastic coupling in the new grain with different orientation. In the specific case of the signal (d-e) in Fig. 2(b), the amplitude drop is associated with the latter case, because the deepest grain has a [0 0 1] orientation and such an orientation preclude TA mode detection.

The 4-D stacked, or slice-by-slice, representations obtained as an output of the slicing offers a mode-by-mode view on the information of each extracted ridge, analogous to a loaf of sliced bread. Looking to such representation from the top gives a view on the first few nanometers of the sample, i.e. the gold-coated surface of the ceria sample [Fig. 3(a-c)]. One can identify the different grains from their associated BF (colors), white zones being attributed to signals with no exploitable results (photodiode saturation and or amplitude of the associated WSST ridge below the -68 dB threshold defined previously). These first layers of the sample reconstructed can be directly compared to the EBSD pattern of the scanned area of the sample. The localizations of the two signals analyzed in Fig. 2 are represented, on these top views, as a green star [Fig. 2(a-c)] and a red circle [Fig. 2(d-h)]. Imaging results [Fig. 3(e-g)], output of the shaping, reconstruct the 3-D boundaries of the grains detected by each modes: the LA mode [Fig. 3(e)] brings out three main grains (1/purple, 2/orange and 3/yellow) while fTA/TA modes interval identifies smaller ones insides these main LA grains. The fTA mode [Fig. 3(f)] deconstruct the 1/purple grain into three smaller ones: 1A/salmon-red, 1B/beige and a third one, 1C, that is evidenced thanks to the absence of detection of the fTA mode. The TA mode [Fig. 3(g)], similarly, deconstruct the 2/orange grain into three smaller ones:

2A/green, 2B/yellow and a third one, 2C, depicted by the absence of TA mode in it. Moreover, part of the 1A grain is reconstructed also with the TA mode as 1A/blue [Fig. 3(g)]. This grain presents the peculiarity of being imaged by the three acoustic quasi-modes: LA (a)-(e), fTA (b)-(f) and sTA (c)-(g) [Fig. 3]. The z-axis (depth) scales are enlarged for better visualization, the ratio between the z-axis and the x- and y-axes are 1/6 in Fig. 3(e) and 1/12 in Fig. 3(f-g). Concerning the axial (depth) resolution, its estimation depends on the acoustic quasi-mode studied, since it is linked to the temporal resolution of the corresponding wavelet in the WSST. However, the acoustic velocity (and hence BF) ratio between the TA waves and the LA ones being close to 2 leads to approximately 0.75 µm resolution for both a LA wave detected at 64 GHz and a TA wave detected at 34 GHz, while the temporal resolution of the wavelet is such that it includes at least 6 full oscillations of the associated BF wavelength.

The use of the alphashape algorithm offers the possibility to estimate the volume of the reconstructed grains (Tab. 2). The uncertainties are obtained using the definition of the alphashape: the radius of the sphere used to shape our voxels clouds is $\frac{1}{\alpha} = 1$ µm thus the volume uncertainty is linked to the volume of the corresponding sphere of radius 1 µm.

Table 2: Volume estimates of the alphashape reconstructed grains.

LA grains	Volume (± 4.2 µm^3)
1 (purple)	1 530
2 (orange)	1 336
3 (yellow)	1 901
fTA grains	**Volume (± 4.2 µm^3)**
1A (salmon-red)	264
1B (beige)	186
TA grains	**Volume (± 4.2 µm^3)**
1A (blue)	97
2A (green)	237
2B (yellow)	344

When detected, the stronger sensitivity to anisotropy of the TA modes offers an imaging contrast that was not achieved by monitoring the LA mode, as evidenced in the upper part of Fig. 3(a-c). Looking to the first slices of the processing, the LA mode results in Fig. 3(a) seems to indicate the presence of three main grains in the scanned area, at the interface gold OAT/CeO_2. The same processing applied to the fTA [Fig. 3(b)] and TA [Fig. 3(c)] modes leads to a new interpretation of the LA mode results, highlighting the presence of smaller grains: the LA purple grain in Fig. 3(a) is in fact composed of three grains, two of them being evidenced by the fTA mode results [Fig. 3(b)], and one of the two being also imaged by monitoring the sTA mode propagation [blue grain in Fig. 3(c)]. In this specific grain, all the three possible acoustic quasi-modes are monitored, offering the possibility to estimate its crystalline orientation in the laboratory frame [78, 79].

Another example of the imaging enhancement permitted by TA modes detection is given in Fig. 3(c) where two grains, that were originally imaged as one grain on the LA mode results [Fig. 3(a)], with close, but different, BF of a TA mode are pictured in green and yellow. One can also deduce the presence of a third grain, 2C, located in the scan interval $x = [0, 5]$ µm and $y = [10, 20]$ µm, not detected in the TA representation (white space in Fig 3(c)), and included in the orange grain on the LA mode results [Fig. 3(a)]. Finally, thanks to the additional information obtained with the TA modes, a complete view of the ceria polycrystal is achieved by TDBS and is in a very good agreement with the EBSD pattern measured on the surface of the sample [Fig. 3(d)]. The imaging contrast provided by the TA modes leads to the detection of the same number of grains as the EBSD pattern. The extension of these observations from the

OAT vicinity to the depth of the grains, with the alphashape 3-D results shown in Fig. 3(e-g), presents the evolution of the grains boundaries with depth. The 3-D representation obtained with the LA mode sheds some light on a small grain appearing only in the depth of the sample (from 6 to 8 µm deep), below the violet one, with a BF close to the interval of the orange grain hence colored in orange in Fig. 3(e). Such deep transition from one grain to another, not visible using electron microscopy without destructive serial section, highlights the capacity of the TDBS technique to image grain microstructure nondestructively in 3D.

3.2. Buried interface inclination estimation

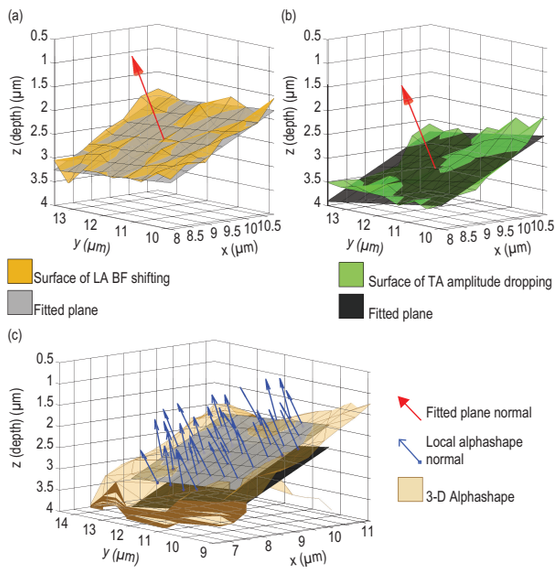

Figure 4: Inclined buried interface analysis. (a) Surface of frequency shifting of the LA mode (orange surface) and best (least mean square) fitted plane (grey plane). (b) Surface of TA mode's ridge amplitude (in the WSST spectrogram) drop below the -68 dB threshold (green surface) and best (least mean square) fitted plane (black plane). The red arrows depict the outward normal of the fitted plane used to estimate the mean inclination angle of the surface. (c) Comparison of the alphashape LA mode results (yellow triangles mesh) and the two fitted planes of (a-b). The blue arrows, with a square base, highlights the local normals used to estimate the averaged angle over the alphashape region. (colors needed)

The 3-D alphashapes results appear as a suitable representation to locate buried inclined interfaces between differently oriented grains. One such surface is found to be between the orange (upper) and yellow (lower) grains of the LA mode alphashape [Fig. 3 (e)], located in the center of the scanned area and between 2 to 3 µm deep. Evidenced by both the LA and one TA modes, the inclination of this interface can be assessed by following the behavior of the TDBS signals in the vicinity of this area, one of the signals being represented in Fig. 2(d). As already mentioned, such signals are sensitive to the crossing of the interface by the acoustic pulse and is evidenced by the frequency shifting of the LA mode and the amplitude drop to the noise level of the TA mode. The situation when a CAP is incident on an inclined boundary between differently oriented grains leads to the reflection and refraction of the CAP (and not of the probe light due to the optical isotropy of ceria), and could lead to the mode-conversion of the incident CAP into up to three reflected and transmitted CAPs with different polarizations [80]. For the interface inclinations observed in this manuscript, the propagation directions of the reflected CAPs deviates more importantly than the directions of the transmitted CAPs, in comparison with the most efficient detection direction, *i.e.*, the propagation direction of the probe light. The reason of these detection reductions is linked to the efficiency of the light scattering by the CAP (acousto-optic interaction), being reduced due to the deviation from the momentum conservation law of the photon-phonon interaction. This deviation from the optimal scattering geometry results in the weakening of the scattering of the probe light and thus of the heterodyne detection, causing a diminution of the amplitude of the TDBS signal. Thus, an abrupt decrease to the noise level of the contribution to the TDBS signal from the reflected CAP is owing to its deviation from the propagation

direction of the probe light (which is about 2θ in weakly elastically anisotropic crystals like ceria), while the transmitted CAP contribution is "only" weakened for the discussed small angles. Considering small angles results in significantly smaller refraction angles of the CAP in comparison with the reflection angles. Because of the low elastic anisotropy of ceria, its Zener ratio being $\alpha_r = 2C_{44}/(C_{11} - C_{12}) = 0.4$ [57], the contribution to the TDBS signal of the mode-converted transmitted CAP is considered confined to the contribution of the transmitted LA mode only. On one hand, low anisotropy could lead to weak mode-conversion, and, on another hand, the resulting transmitted TA waves would be composed in minority of a longitudinal component, which is the component efficiently scattering the probe light for the heterodyne detection, and in majority of transversal components, efficiently depolarizing the probe light, *i.e.*, precluding it for being detected. In conclusion, for the experiments reported in this manuscript, the contributions to the TDBS signal of the reflected and the mode-converted transmitted TA waves are considered to be too small to be accounted for, even thought they are existing.

A representation of the buried surface at which the frequency shifting in the LA occurs is shown in Fig. 4(a). Similarly, a representation of the buried surface at which the amplitude drops for the TA mode is shown in Fig. 4(b). Note that the absolute depth at which the buried surface is find from LA and TA mode are slightly shifted, due to the blind zone in the first ps of the temporal signals, while this is not influencing the inclination angle recovery. Fitting the least-mean square plane to each surface gives access to a plane from which the mean inclination angle (with respect to the gold OAT, z=0 µm plane) is estimated via its outward normal. Results obtained from the frequency shifting of the LA mode [Fig. 4(a)] gives 23.3°, and from the amplitude drop of the TA mode [Fig. 4(b)] gives 23.2°. Comparisons of the alphashape result of the lower grain of the interface with the fitted planes shown in Fig. 4(a) (LA mode) and Fig. 4(b) (TA mode) are shown in Fig. 4(c). A good agreement between the inclinations of the fitted plane and the actual alphashape result is shown. The local normals of the alphashape's triangle mesh of the same area are determined (blue arrows) and the averaged angle between these local normals and the gold OAT gives a 23.8° inclined interface. Hence a good agreement between the fitted planes to the LA and TA modes surfaces, and the alphashape reconstruction, allows estimation of the inclination of this interface to be of about 23.5 ± 0.5° with respect to the z=0 µm plane.

4. Conclusions

A method to reconstruct the 3-D grains boundaries of a polycrystalline ceria (CeO_2) sample, down to 8 µm depth, from opto-acousto-optic measurements, has been implemented. This technique provides opportunity to recreate an accurate 3-D image of grains and their respective boundaries. Time frequency tools are developed for the reconstruction of the temporal contribution to the measured signal of each possible acoustic mode independently. Grain boundary identification has been enhanced by monitoring of the acoustic quasi-transverse modes, highlighting boundaries that were not visible via quasi-longitudinal mode detection only. This new signal processing method opens the possibility of non-destructive, *in situ* visualization of grain shape and its evolution beneath the surface. The angle of a buried inclined interface between two differently oriented grains is estimated to be about 23.5°. Extraction of such fundamental information (size and orientation) has application in the characterization of in-situ/real-time microstructure evolution in extreme environments including high temperature and pressure, high magnetic and electric fields, and harsh irradiation environments.

Acknowledgments

This research is supported by the Public education service and research of France, the French National Centre for Scientific Research, the Agence Nationale de la Recherche [project <ANR18-CE42-I2T2M>], the Acoustic Hub® program, and the Région Pays de la Loire via RFI Le Mans Acoustique (LMAc) [project OPACOP 2018]. DHH and ZH acknowledge support from the Center for Thermal Energy Transport, an

Energy Frontier Research Center funded by the US Department of Energy, Office of Science, Office of Basic Energy Sciences. The authors wish to thank C. MECHRI for suggesting the use of wavelets and L. SIMON for discussions and references on the wavelet synchro-squeezed transform. We thank our colleagues from NETA who provided insight and expertise that greatly assisted the research.

Author contributions

S.R., S.A., N.C., V.T., D.H.H. and V.E.G. designed the research, D.H.H. and Z.H. prepared the sample, E.L.S., S.R., S.A., N.C. and D.H.H. contributed to the experiments, T.T. and S.R. contributed to signal processing, T.T., S.R., N.C., V.T., D.H.H. and V.E.G. analysed and interpreted the experimental observations, T.T., S.R., D.H.H. and V.E.G. wrote the manuscript. All authors reviewed the manuscript.

Conflicts of Interests

The authors declare no competing financial interests.

References

[1] A. G. Bell, On the production and reproduction of sound by light, American Journal of Science s3-20 (118) (1880) 305–324. doi:10.2475/ajs.s3-20.118.305.

[2] A. Rosencwaig, Photoacoustic Spectroscopy of Biological Materials, Science 181 (4100) (1973) 657–658. doi:10.1126/science.181.4100.657.

[3] A. Rosencwaig, P. R. Griffiths, Photoacoustics and Photoacoustic Spectroscopy, Physics Today 34 (6) (2008) 64. doi:10.1063/1.2914619.

[4] V. Ė. Gusev, A. A. Karabutov, Laser Optoacoustics, New York : American Institute of Physics, 1993, translation of: Lazernai͡a optoakustika.

[5] F. A. McDonald, Photoacoustic, photothermal, and related techniques: A review, Canadian Journal of Physicsdoi:10.1139/p86-174.

[6] C. B. Scruby, L. E. Drain, Laser Ultrasonics Techniques and Applications, CRC Press, 1990.

[7] F. Lepoutre, Coupled equations of modulated photothermal effects, hypotheses and solutions, Le Journal de Physique Colloques 44 (C6) (1983) C6–3–C6–8. doi:10.1051/jphyscol:1983601.

[8] B. Cretin, Super-résolution en microscopie photothermique et thermoélastique: extension du concept de champ proche, Revue Générale de Thermique 37 (7) (1998) 556–564. doi:10.1016/S0035-3159(98)80034-2.

[9] D. Fournier, B. C. Forget, C. Boué, J. P. Roger, Micron scale photothermal imaging1Based on a paper presented as a plenary talk at Eurotherm Seminar No. 57 “Microscale Heat Transfer”, Poitiers, France, July 8–10, 1998.1, International Journal of Thermal Sciences 39 (4) (2000) 514–518. doi:10.1016/S1290-0729(00)00230-1.

[10] J. M. Atkin, S. Berweger, A. C. Jones, M. B. Raschke, Nano-optical imaging and spectroscopy of order, phases, and domains in complex solids, Advances in Physics 61 (6) (2012) 745–842. doi:10.1080/00018732.2012.737982.

[11] D. H. Hurley, Pump-Probe Laser Ultrasonics: Characterization of Material Microstructure, IEEE Nanotechnology Magazine 13 (3) (2019) 29–38. doi:10.1109/MNANO.2019.2904772.

[12] S. Manohar, R. G. H. Willemink, F. van der Heijden, C. H. Slump, T. G. van Leeuwen, Concomitant speed-of-sound tomography in photoacoustic imaging, Applied Physics Letters 91 (13) (2007) 131911. doi:10.1063/1.2789689.

[13] G. Rousseau, A. Blouin, J.-P. Monchalin, Non-contact photoacoustic tomography and ultrasonography for tissue imaging, Biomedical Optics Express 3 (1) (2012) 16–25. doi:10.1364/BOE.3.000016.

[14] T. F. Fehm, X. L. Deán-Ben, D. Razansky, Four dimensional hybrid ultrasound and optoacoustic imaging via passive element optical excitation in a hand-held probe, Applied Physics Letters 105 (17) (2014) 173505. doi:10.1063/1.4900520.

[15] G. Wurzinger, R. Nuster, G. Paltauf, Combined photoacoustic, pulse-echo laser ultrasound, and speed-of-sound imaging using integrating optical detection, Journal of Biomedical Optics 21 (8) (2016) 086010. doi:10.1117/1.JBO.21.8.086010.

[16] C. Thomsen, J. Strait, Z. Vardeny, H. J. Maris, J. Tauc, J. J. Hauser, Coherent Phonon Generation and Detection by Picosecond Light Pulses, Physical Review Letters 53 (10) (1984) 989–992. doi:10.1103/PhysRevLett.53.989.

[17] H. T. Grahn, H. J. Maris, J. Tauc, Picosecond ultrasonics, IEEE Journal of Quantum Electronics 25 (12) (1989) 2562–2569. doi:10.1109/3.40643.

[18] O. Matsuda, M. C. Larciprete, R. Li Voti, O. B. Wright, Fundamentals of picosecond laser ultrasonics, Ultrasonics 56 (2015) 3–20. doi:10.1016/j.ultras.2014.06.005.

[19] E. F. Carome, N. A. Clark, C. E. Moeller, Generation of acoustic signals in liquids by ruby laser-induced thermal stress transients, Applied Physics Letters 4 (6) (1964) 95–97. doi:10.1063/1.1753985.

[20] F. W. Cross, R. K. Al-Dhahir, P. E. Dyer, A. J. MacRobert, Time-resolved photoacoustic studies of vascular tissue ablation at three laser wavelengths, Applied Physics Letters 50 (15) (1987) 1019–1021. doi:10.1063/1.97994.

[21] A. A. Oraevsky, R. O. Esenaliev, S. L. Jacques, F. K. Tittel, Laser optic-acoustic tomography for medical diagnostics: Principles, in: Biomedical Sensing, Imaging, and Tracking Technologies I, Vol. 2676, International Society for Optics and Photonics, 1996, pp. 22–31. doi:10.1117/12.238786.

[22] A. Karabutov, N. B. Podymova, V. S. Letokhov, Time-resolved laser optoacoustic tomography of inhomogeneous media, Applied Physics B 63 (6) (1996) 545–563. doi:10.1007/BF01830994.

[23] A. A. Oraevsky, V. A. Andreev, A. A. Karabutov, R. O. Esenaliev, Two-dimensional optoacoustic tomography: Transducer array and image reconstruction algorithm, in: Laser-Tissue Interaction X: Photochemical, Photothermal, and Photomechanical, Vol. 3601, International Society for Optics and Photonics, 1999, pp. 256–267. doi:10.1117/12.350007.

[24] V. Ntziachristos, J. Ripoll, L. V. Wang, R. Weissleder, Looking and listening to light: The evolution of whole-body photonic imaging, Nature Biotechnology 23 (3) (2005) 313–320. doi:10.1038/nbt1074.

[25] P. Beard, Biomedical photoacoustic imaging, Interface Focus 1 (4) (2011) 602–631. doi:10.1098/rsfs.2011.0028.

[26] C. Lutzweiler, D. Razansky, Optoacoustic imaging and tomography: Reconstruction approaches and outstanding challenges in image performance and quantification, Sensors (Basel, Switzerland) 13 (6) (2013) 7345–7384. doi:10.3390/s130607345.

[27] L. V. Wang, L. Gao, Photoacoustic Microscopy and Computed Tomography: From Bench to Bedside, Annual Review of Biomedical Engineering 16 (1) (2014) 155–185. doi:10.1146/annurev-bioeng-071813-104553.

[28] A. Taruttis, V. Ntziachristos, Advances in real-time multispectral optoacoustic imaging and its applications, Nature Photonics 9 (4) (2015) 219–227. doi:10.1038/nphoton.2015.29.

[29] L. V. Wang, J. Yao, A practical guide to photoacoustic tomography in the life sciences, Nature Methods 13 (8) (2016) 627–638. doi:10.1038/nmeth.3925.

[30] G. Wissmeyer, M. A. Pleitez, A. Rosenthal, V. Ntziachristos, Looking at sound: Optoacoustics with all-optical ultrasound detection, Light: Science & Applications 7 (1) (2018) 53. doi:10.1038/s41377-018-0036-7.

[31] I. Steinberg, D. M. Huland, O. Vermesh, H. E. Frostig, W. S. Tummers, S. S. Gambhir, Photoacoustic clinical imaging, Photoacoustics 14 (2019) 77–98. doi:10.1016/j.pacs.2019.05.001.

[32] L. V. Wang, S. Hu, Photoacoustic Tomography: In Vivo Imaging from Organelles to Organs, Science 335 (6075) (2012) 1458–1462. doi:10.1126/science.1216210.

[33] G. Ku, L. V. Wang, Deeply penetrating photoacoustic tomography in biological tissues enhanced with an optical contrast agent, Optics Letters 30 (5) (2005) 507–509. doi:10.1364/OL.30.000507.

[34] C. Thomsen, H. Grahn, H. Maris, J. Tauc, Picosecond interferometric technique for study of phonons in the brillouin frequency range, Optics Communications 60 (1-2) (1986) 55–58. doi:10.1016/0030-4018(86)90116-1.

[35] H. N. Lin, R. J. Stoner, H. J. Maris, J. Tauc, Phonon attenuation and velocity measurements in transparent materials by picosecond acoustic interferometry, Journal of Applied Physics 69 (7) (1991) 3816–3822. doi:10.1063/1.348958.

[36] V. Gusev, P. Ruello, Advances in applications of time-domain Brillouin scattering for nanoscale imaging, Applied Physics Reviews 5 (3) (2018) 031101. doi:10.1063/1.5017241.

[37] C. Rossignol, J. M. Rampnoux, M. Perton, B. Audoin, S. Dilhaire, Generation and Detection of Shear Acoustic Waves in Metal Submicrometric Films with Ultrashort Laser Pulses, Physical Review Letters 94 (16) (2005) 166106. doi:10.1103/PhysRevLett.94.166106.

[38] T. Dehoux, K. Ishikawa, P. H. Otsuka, M. Tomoda, O. Matsuda, M. Fujiwara, S. Takeuchi, I. A. Veres, V. E. Gusev, O. B. Wright, Optical tracking of picosecond coherent phonon pulse focusing inside a submicron object, Light: Science & Applications 5 (5) (2016) e16082–e16082. doi:10.1038/lsa.2016.82.

[39] S. M. Nikitin, V. Tournat, N. Chigarev, A. Bulou, B. Castagnede, A. Zerr, V. Gusev, Directivity patterns and pulse profiles of ultrasound emitted by laser action on interface between transparent and opaque solids: Analytical theory, Journal of Applied Physics 115 (4) (2014) 044902. doi:10.1063/1.4861882.

[40] O. B. Wright, Thickness and sound velocity measurement in thin transparent films with laser picosecond acoustics, Journal of Applied Physics 71 (4) (1992) 1617–1629. doi:10.1063/1.351218.

[41] K. E. O'Hara, X. Hu, D. G. Cahill, Characterization of nanostructured metal films by picosecond acoustics and interferometry, Journal of Applied Physics 90 (9) (2001) 4852–4858. doi:10.1063/1.1406543.

[42] A. Devos, R. Côte, Strong oscillations detected by picosecond ultrasonics in silicon: Evidence for an electronic-structure effect, Physical Review B 70 (12) (2004) 125208. doi:10.1103/PhysRevB.70.125208.

[43] A. Devos, R. Côte, G. Caruyer, A. Lefèvre, A different way of performing picosecond ultrasonic measurements in thin transparent films based on laser-wavelength effects, Applied Physics Letters 86 (21) (2005) 211903. doi:10.1063/1.1929869.

[44] F. Hudert, A. Bartels, T. Dekorsy, K. Köhler, Influence of doping profiles on coherent acoustic phonon detection and generation in semiconductors, Journal of Applied Physics 104 (12) (2008) 123509. doi:10.1063/1.3033140.

[45] C. Mechri, P. Ruello, J. M. Breteau, M. R. Baklanov, P. Verdonck, V. Gusev, Depth-profiling of elastic inhomogeneities in transparent nanoporous low-k materials by picosecond ultrasonic interferometry, Applied Physics Letters 95 (9) (2009) 091907. doi:10.1063/1.3220063.

[46] A. M. Lomonosov, A. Ayouch, P. Ruello, G. Vaudel, M. R. Baklanov, P. Verdonck, L. Zhao, V. E. Gusev, Nanoscale Noncontact Subsurface Investigations of Mechanical and Optical Properties of Nanoporous Low- k Material Thin Film, ACS Nano 6 (2) (2012) 1410–1415. doi:10.1021/nn204210u.

[47] A. Steigerwald, Y. Xu, J. Qi, J. Gregory, X. Liu, J. K. Furdyna, K. Varga, A. B. Hmelo, G. Lüpke, L. C. Feldman, N. Tolk, Semiconductor point defect concentration profiles measured using coherent acoustic phonon waves, Applied Physics Letters 94 (11) (2009) 111910. doi:10.1063/1.3099341.

[48] D. Yarotski, E. Fu, L. Yan, Q. Jia, Y. Wang, A. J. Taylor, B. P. Uberuaga, Characterization of irradiation damage distribution near TiO2/SrTiO3 interfaces using coherent acoustic phonon interferometry, Applied Physics Letters 100 (25) (2012) 251603. doi:10.1063/1.4729621.

[49] J. Gregory, A. Steigerwald, H. Takahashi, A. Hmelo, N. Tolk, Erratum: "Ion implantation induced modification of optical properties in single-crystal diamond studied by coherent acoustic phonon spectroscopy" [Appl. Phys. Lett. 101, 181904 (2012)], Applied Physics Letters 103 (4) (2013) 049904. doi:10.1063/1.4816967.

[50] S. M. Nikitin, N. Chigarev, V. Tournat, A. Bulou, D. Gasteau, B. Castagnede, A. Zerr, V. E. Gusev, Revealing sub-Mm and Mm-scale textures in H 2 O ice at megabar pressures by time-domain Brillouin scattering, Scientific Reports 5 (1) (2015) 1–11. doi:10.1038/srep09352.

[51] M. Kuriakose, S. Raetz, N. Chigarev, S. M. Nikitin, A. Bulou, D. Gasteau, V. Tournat, B. Castagnede, A. Zerr, V. E. Gusev, Picosecond laser ultrasonics for imaging of transparent polycrystalline materials compressed to megabar pressures, Ultrasonics 69 (2016) 259–267. doi:10.1016/j.ultras.2016.03.007.

[52] C. Rossignol, N. Chigarev, M. Ducousso, B. Audoin, G. Forget, F. Guillemot, M. C. Durrieu, In Vitro picosecond ultrasonics in a single cell, Applied Physics Letters 93 (12) (2008) 123901. doi:10.1063/1.2988470.

[53] S. Danworaphong, M. Tomoda, Y. Matsumoto, O. Matsuda, T. Ohashi, H. Watanabe, M. Nagayama, K. Gohara, P. H. Otsuka, O. B. Wright, Three-dimensional imaging of biological cells with picosecond ultrasonics, Applied Physics Letters 106 (16) (2015) 163701. doi:10.1063/1.4918275.

[54] F. Pérez-Cota, R. J. Smith, E. Moradi, L. Marques, K. F. Webb, M. Clark, High resolution 3D imaging of living cells with sub-optical wavelength phonons, Scientific Reports 6 (1) (2016) 39326. doi:10.1038/srep39326.

[55] I. Chaban, H. D. Shin, C. Klieber, R. Busselez, V. E. Gusev, K. A. Nelson, T. Pezeril, Time-domain Brillouin scattering for the determination of laser-induced temperature gradients in liquids, Review of Scientific Instruments 88 (7) (2017) 074904. doi:10.1063/1.4993132.

[56] M. Khafizov, J. Pakarinen, L. He, H. Henderson, M. Manuel, A. Nelson, B. Jaques, D. Butt, D. Hurley, Subsurface imaging of grain microstructure using picosecond ultrasonics, Acta Materialia 112 (2016) 209–215. doi:10.1016/j.actamat.2016.04.003.

[57] Y. Wang, D. H. Hurley, Z. Hua, G. Sha, S. Raetz, V. E. Gusev, M. Khafizov, Nondestructive characterization of polycrystalline 3D microstructure with time-domain Brillouin scattering, Scripta Materialia 166 (2019) 34–38. doi:10.1016/j.scriptamat.2019.02.037.

[58] Y. Wang, D. H. Hurley, Z. Hua, T. Pezeril, S. Raetz, V. E. Gusev, V. Tournat, M. Khafizov, Imaging grain microstructure in a model ceramic energy material with optically generated coherent acoustic phonons, Nature Communications 11 (1) (2020) 1597. doi:10.1038/s41467-020-15360-3.

[59] D. H. Hurley, O. B. Wright, O. Matsuda, T. Suzuki, S. Tamura, Y. Sugawara, Time-resolved surface acoustic wave propagation across a single grain boundary, Physical Review B 73 (12) (2006) 125403. doi:10.1103/PhysRevB.73.125403.

[60] F.-C. Chiu, C.-M. Lai, Optical and electrical characterizations of cerium oxide thin films, Journal of Physics D: Applied Physics 43 (7) (2010) 075104. doi:10.1088/0022-3727/43/7/075104.

[61] NETA, https://www.neta-tech.com/fr/.

[62] A. Bartels, F. Hudert, C. Janke, T. Dekorsy, K. Köhler, Femtosecond time-resolved optical pump-probe spectroscopy at kilohertz-scan-rates over nanosecond-time-delays without mechanical delay line, Applied Physics Letters 88 (4) (2006) 041117. doi:10.1063/1.2167812.

[63] A. Abbas, Y. Guillet, J.-M. Rampnoux, P. Rigail, E. Mottay, B. Audoin, S. Dilhaire, Picosecond time resolved opto-acoustic imaging with 48 MHz frequency resolution, Optics Express 22 (7) (2014) 7831. doi:10.1364/OE.22.007831.

[64] V. Gusev, A. M. Lomonosov, P. Ruello, A. Ayouch, G. Vaudel, Depth-profiling of elastic and optical inhomogeneities in transparent materials by picosecond ultrasonic interferometry: Theory, Journal of Applied Physics 110 (12) (2011) 124908. doi:10.1063/1.3665646.

[65] I. L. Fabelinskii, Molecular Scattering of Light, Springer US, 1968. doi:10.1007/978-1-4684-1740-1.

[66] J. G. Dil, Brillouin scattering in condensed matter, Reports on Progress in Physics 45 (3) (1982) 285–334. doi:10.1088/0034-4885/45/3/002.

[67] Y. Wang, M. Khafizov, Shear wave generation by mode conversion in picosecond ultrasonics: Impact of grain orientation and material properties, Journal of the American Ceramic Society n/a (n/a). doi:10.1111/jace.17654.

[68] I. Daubechies, J. Lu, H.-T. Wu, Synchrosqueezed wavelet transforms: An empirical mode decomposition-like tool, Applied and Computational Harmonic Analysis 30 (2) (2011) 243–261. doi:10.1016/j.acha.2010.08.002.

[69] F. Auger, P. Flandrin, Y.-T. Lin, S. McLaughlin, S. Meignen, T. Oberlin, H.-T. Wu, Time-Frequency Reassignment and Synchrosqueezing: An Overview, IEEE Signal Processing Magazine 30 (6) (2013) 32–41. doi:10.1109/MSP.2013.2265316.

[70] S. Meignen, D.-H. Pham, S. Mclaughlin, On Demodulation, Ridge Detection and Synchrosqueezing for Multicomponent Signals, IEEE Transactions on Signal Processing 65 (8) (2017) 2093–2103. doi:10.1109/TSP.2017.2656838.

[71] S. Meignen, T. Oberlin, D.-H. Pham, Synchrosqueezing transforms: From low- to high-frequency modulations and perspectives, Comptes Rendus Physique 20 (5) (2019) 449–460. doi:10.1016/j.crhy.2019.07.001.

[72] G. Thakur, E. Brevdo, N. S. Fučkar, H.-T. Wu, The Synchrosqueezing algorithm for time-varying spectral analysis: Robustness properties and new paleoclimate applications, Signal Processing 93 (5) (2013) 1079–1094. doi:10.1016/j.sigpro.2012.11.029.

[73] F. Bause, B. Henning, B. Huang, A. Kunoth, Ultrasonic waveguide signal decomposition using the synchrosqueezed wavelet transform for modal group delay computation, in: 2013 IEEE International Ultrasonics Symposium (IUS), 2013, pp. 671–674. doi:10.1109/ULTSYM.2013.0173.

[74] B. Hazra, A. Sadhu, S. Narasimhan, Fault detection of gearboxes using synchro-squeezing transform, Journal of Vibration and Control 23 (19) (2017) 3108–3127. doi:10.1177/1077546315627242.

[75] N. Otsu, A Threshold Selection Method from Gray-Level Histograms, IEEE Transactions on Systems, Man, and Cybernetics 9 (1) (1979) 62–66. doi:10.1109/TSMC.1979.4310076.

[76] H. Edelsbrunner, D. Kirkpatrick, R. Seidel, On the shape of a set of points in the plane, IEEE Transactions on Information Theory 29 (4) (1983) 551–559. doi:10.1109/TIT.1983.1056714.

[77] H. Edelsbrunner, E. P. Mücke, Three-dimensional alpha shapes, ACM Transactions on Graphics 13 (1) (1994) 43–72. doi:10.1145/174462.156635.

[78] D. Y. Chung, V. Konecny, The determination of the orientation of cubic crystals from measured sound velocities, physica status solidi (a) 52 (1) (1979) 29–33. doi:10.1002/pssa.2210520103.

[79] A. Duda, T. Paszkiewicz, Application of ultrasonic measurements to determine the orientation of crystalline samples, Physica B: Condensed Matter 316-317 (2002) 118–121. doi:10.1016/S0921-4526(02)00436-2.

[80] V. E. Gusev, T. Thréard, D. H. Hurley, S. Raetz, Theory of time-domain Brillouin scattering for probe light and acoustic beams propagating at an arbitrary relative angle: Application to acousto-optic interaction near material interfaces, arXiv:2107.05294 [cond-mat, physics:physics]arXiv:2107.05294.

[81] D. Royer, E. Dieulesaint, Elastic Waves in Solids I: Free and Guided Propagation, Springer Science & Business Media, 1999.

Supplementary Materials

Supplementary materials on the 3-D slowness surfaces of ceria (CeO_2) and optical refractive index estimation

Up to three acoustic quasi-modes can be generated in the cubic polycrystal CeO_2. The determination of the associated BF intervals requires the estimation of the fastest and slowest acoustic velocities for each quasi mode. To achieve this, the Christoffel equation is solved and the velocities v associated to any direction are given by the roots of the secular equation (following Ref. [81] - Chapter 4 notation):

$$|\Gamma_{ij} - \rho v^2 \delta_{il}| = 0, \tag{2}$$

with Γ_{ij} Christoffel's tensor, ρ ceria's density and δ_{ij} the Kronecker symbol. The elastic constants (C_{11} = 451 GPa, C_{12} = 119 GPa and C_{44} = 66 GPa) and the density $\rho = 7.22$ g cm^{-3} are given in Ref. [57]. The 3-D slowness (inverse of velocity) surfaces of the three quasi-modes are plotted in Fig. 5 which shows how much faster the LA waves (inside surface - red) are compared to both TA ones. The slowness surfaces also clearly depict that both TA modes are more sensitive to changes in the propagation direction with respect to the crystal principal axes than the LA mode. The results of table 1 are obtained by applying Eq. 1 to the fastest and slowest velocities of each mode, leading to the presented estimates of the BF intervals.

Determination of the optical refractive index n, of our ceria sample, to the probe wavelength λ= 535 nm is made possible thanks to the detection of the three acoustic quasi mode in a specific grain of the area scanned, located in the spatial interval x = [0, 5] µm, y = [20, 25] µm, 1A in Fig. 3. Indeed, from the slowness surfaces, it is possible to represent the two "surfaces of shear velocity ratio to LA" for the two TA modes [Fig. 6]. In Eq. 1, λ and n are fixed, thus the ratio of velocities is equal to the ratios of the BFs. These two ratios are used to locate, in the two "surfaces of shear velocity ratio to LA" the possible orientations and thus the associated acoustic velocities. Finally, by isolating n in Eq. 1, the optical refractive index can be estimated for the probe wavelength. Table 3 gives the values obtained with their associated uncertainties given by the frequency resolution of the ridge extracted in the WSST, the BF interval being associated to the corresponding frequency bin in the histogram of the segmentation method (see next section for more explanations).

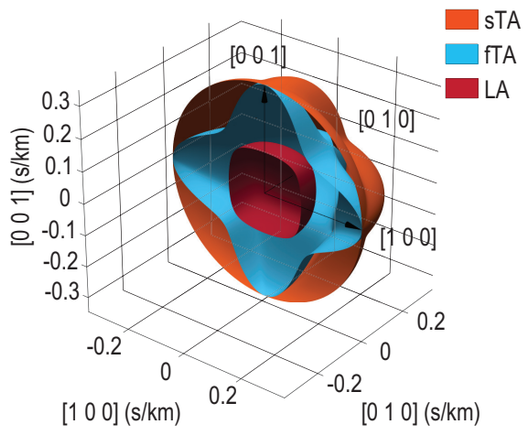

Figure 5: 3-D slowness surfaces of the three possible acoustic quasi-modes to propagate in CeO_2. Half of the polar angles are represented to obtain the cross-sectional view. (colors needed)

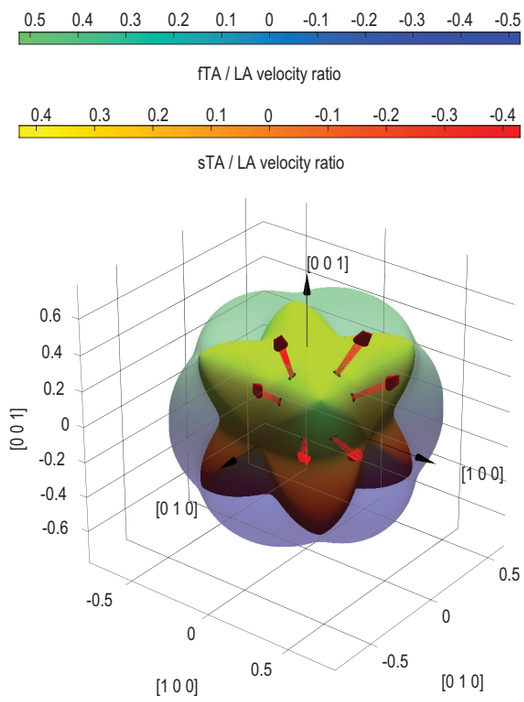

Figure 6: 3-D surfaces of shear velocity ratio to LA. The fTA/LA velocity ratio surface is transparent for better visualization of the sTA/LA one. The possible orientations of the grain 1A, in which the 3 acoustic quasi-modes are monitored, are represented by red arrows (with black circle basis) in 1/8 of the surface. Due to symmetries in the cubic crystalline structure, 6 orientations with common velocity ratio are obtained. (colors needed)

Table 3: Ceria's optical refractive index estimation.

Acoustic mode	Frequency (GHz)	Ratio (to LA)	Associated v ($\mathrm{m\,s^{-1}}$)	Deduced n
LA	61.65 ± 0.47	/	$6\,958 \pm 52$	2.37 ± 0.04
sTA	30.37 ± 0.23	0.4925 ± 0.008	$3\,428 \pm 33$	2.37 ± 0.03
fTA	40.15 ± 0.3	0.6515 ± 0.01	$4\,537 \pm 97$	2.37 ± 0.07

Supplementary materials on histogram segmentation inspired by Otsu's work for grains identification

Originally, Otsu's segmentation method [75] was used in image processing to separate foreground and background using the grayscale of an image.

Each pixel of the image is converted into an intensity value between one and 256 and then the histogram repartition of the intensity is plotted. To separate the background pixels from the foreground ones, a threshold in the [1, 256] intensity scale is obtained automatically by finding the location of the maximum value of the variance between the histogram's bins. This segmentation of the histogram, between the pixels

that contribute to the foreground and the ones that contribute to the background, splits the histogram in two equivalent parts with one threshold. Inspired by this method, the histogram repartition of the voxels, from the 4-D "sliced" output of the slicing post-processing part (Sec. 2.4), is plotted for each acoustic quasi-mode. The bin number and frequency edges are defined by the frequency resolution of the wavelet synchro-squeezed transform, thus defined by the wavelet filter bank used to compute the continuous wavelet transform prior to synchrosqueezing. Such parameter is controlled by the "number of voices per octave" defined in MATLAB's documentation on the continuous wavelet transform. In our specific case, the aim is to locate the frequency intervals containing high occurrence bins. A grain is defined by a volume that contains a considerable amount of voxels having the same BF.

First, a threshold is defined as 5% of the total voxel amount in the histogram (solid red horizontal curve in Fig. 7), and the local maxima (red arrows in Fig. 7) are obtained by looking for peaks in the curve passing through all the bins (black solid curve in Fig. 7) having a prominence higher than half the threshold. Depending on the distribution of the bins surrounding the local maxima, two scenarios are possible. First, if the occupancies of the two surrounding bins are below the threshold, the BF interval defining this grain include the three bins. This case can be observed in the two high BF intervals in Fig. 7(a), and the low BF interval in Fig. 7(c). Secondly, if the surrounding bins have an occupancy above the 5% threshold, then closer attention needs to be given to the voxels repartition. If only one neighbouring bin is higher than the threshold, then the BF interval is shifted compared to the interval centred on the local maxima, along the frequency axis, in a direction towards the neighbouring bin with occupancy higher than the threshold. Such a situation is depicted by the low frequency BF interval in Fig. 7(a). Finally, if all the occupancies of all the neighbouring bins are above the threshold, the gradient of the occupancy curve is computed and is used to locally separate the two highest bins, and split in two BF intervals, hence in two grains, like in the case of the fTA mode depicted in Fig. 7(b). The final BF intervals defining the grains of our ceria scan are depicted by vertical dashed green lines in Figs. 7, and the associated values are gathered in table 4.

Each bin with occupancy above the threshold value could have been treated separately but would have finally appeared, from the alphashape output, as enveloping each other like the different layers of an onion. This could be justified by the fact that, when the BF is estimated close to a boundary between two grains, it could be slightly shifted due to the finite width of the window used for processing.

Table 4: Ceria's grain intervals determined.

LA mode	Frequency (GHz)
LA 1	[61.19 ; 63.05]
LA 2	[64.91 ; 66.77]
LA 3	[67.70 ; 69.56]
fTA mode	**Frequency (GHz)**
fTA 1	[38.5 ; 40.18]
fTA 2	[40.18 ; 41.30]
TA mode	**Frequency (GHz)**
TA 1	[29.76 ; 30.70]
TA 2	[31.64 ; 33.05]
TA 3	[33.05 ; 33.99]

Supplementary materials on the depth of imaging limitations

Grains 3-D imaging results obtained in Fig. 3 appear to be imaged down to a depth of about 8 µm deep in the best cases. This limitation of the depth of imaging can be attributed to the coherence length of the probe laser beam, rather than other physical mechanisms such as the acoustic wave attenuation or the probe

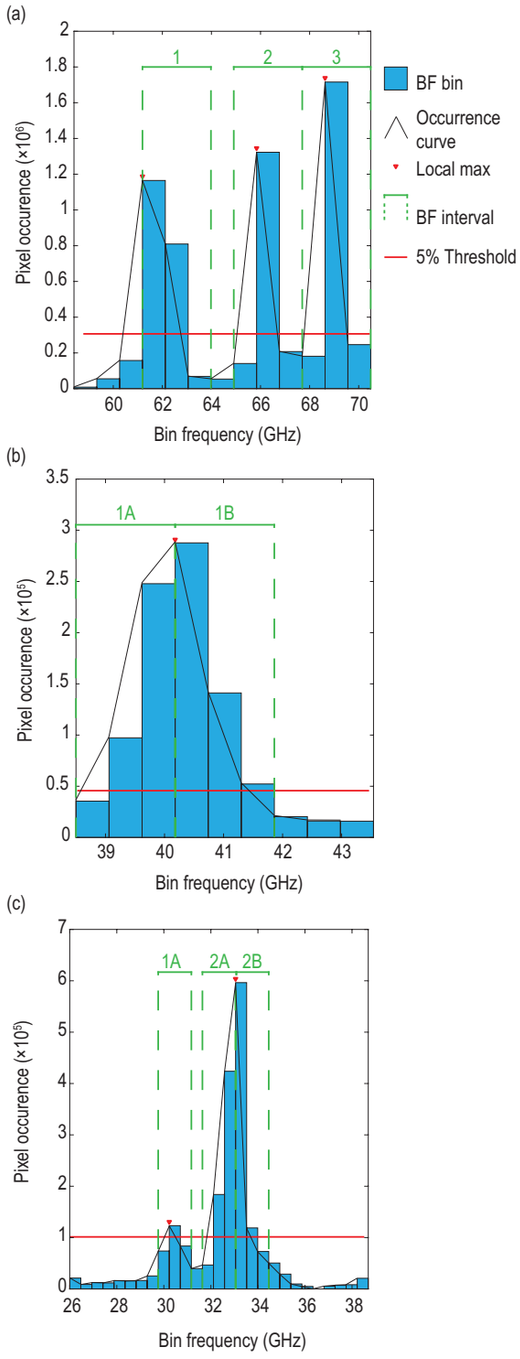

Figure 7: Histograms of the voxels repartition for each acoustic quasi mode: (a) LA, (b) fTA and (c) TA. (colors needed)

laser beam diffraction. To estimate the coherence length of the probe laser beam, one of the acoustic signals with the longest duration is selected (located at the position $x = 25.79$ µm and $y = 23.45$ µm of the scan), and a sinusoid with Gaussian and exponential dampings model is fitted to it. The model is given as:

$$\mathrm{A}\ \sin\left(2\pi f_{\mathrm{B}}^{\mathrm{LA}}\mathrm{t}+\phi\right)\ \exp\left(-2\left(\frac{\mathrm{t}}{\tau_{\mathrm{c}}}\right)^{2}\right)\ \exp\left(-\alpha\mathrm{t}\right), \tag{3}$$

with A the amplitude, $f_{\mathrm{B}}^{\mathrm{LA}} = 61.52$ GHz the BF of the LA mode obtained from the Fourier transform of the full acoustic signal, ϕ the phase, τ_{c} the coherence time of the probe laser pulse and α the acoustic absorption coefficient, of the signal.

Estimation of the coherence time from the fitting gives $\tau_{\mathrm{c}} = 1.16 \pm 0.012$ ns, the uncertainty being estimated with the 95% confidence interval of the fitting. Such a value can be checked from the relation between the coherence time and the duration of the probe laser pulse τ_{probe}:

$$\tau_{\mathrm{probe}} = \frac{2v_{LA}\tau_{\mathrm{c}}}{\mathrm{c}_0/n}, \tag{4}$$

with $v_{\mathrm{LA}} = (f_B^{LA}\lambda)/(2n) = 6\,944$ m.s^{-1} the LA mode velocity, deduced from Eq. 1, and c_0 the speed of light

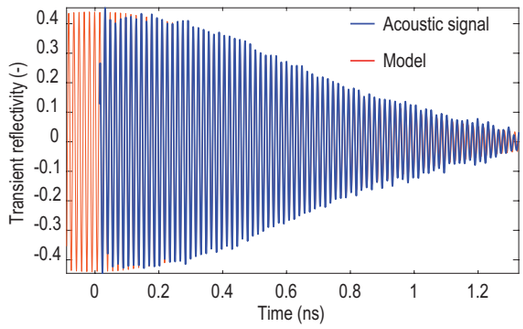

Figure 8: Comparison between the acoustic contribution to the transient reflectivity signal measured by the photodiode, located at the position $x = 25.79$ μm and $y = 23.45$ μm of the scan, and the Gaussian damping model signal obtained by fitting. (colors needed)

in vacuum. The probe laser pulses duration is thus estimated as $\tau_{\mathrm{probe}} = 127 \pm 2$ fs, close enough to the laser datasheet $\tau_{\mathrm{probe}} = 130$ fs. Finally to estimate the coherence penetration depth, one can either estimate the product of the coherence time τ_{c} by the LA mode velocity v_{LA}, giving $L_{\mathrm{c}}^{\mathrm{probe}} = 8.05 \pm 0.08$ µm, or use the estimated duration of the probe laser beam τ_{probe} with:

$$L_{\mathrm{c}}^{\mathrm{probe}} = \frac{(\mathrm{c}_0/n)\tau_{\mathrm{probe}}}{2}. \tag{5}$$

From this second method, the estimated coherence penetration depth is evaluated as $L_{\mathrm{c}}^{\mathrm{probe}} = 8.04 \pm 0.13$ µm, close to the previous estimate and in good agreement with the deepest observed 3-D images of the grain in the main text. The obtained fit is not improved by including the acoustic absorption since the fitted value for α is going to zero when not limited with a lower physical bound equal to 0. Hence the limiting factor for the depth of imaging arise from the penetration depth of the probe laser beam coherence.